Volume 12
Number 16
28 April 2020
Pages 8585-9286

Nanoscale

rsc.li/nanoscale

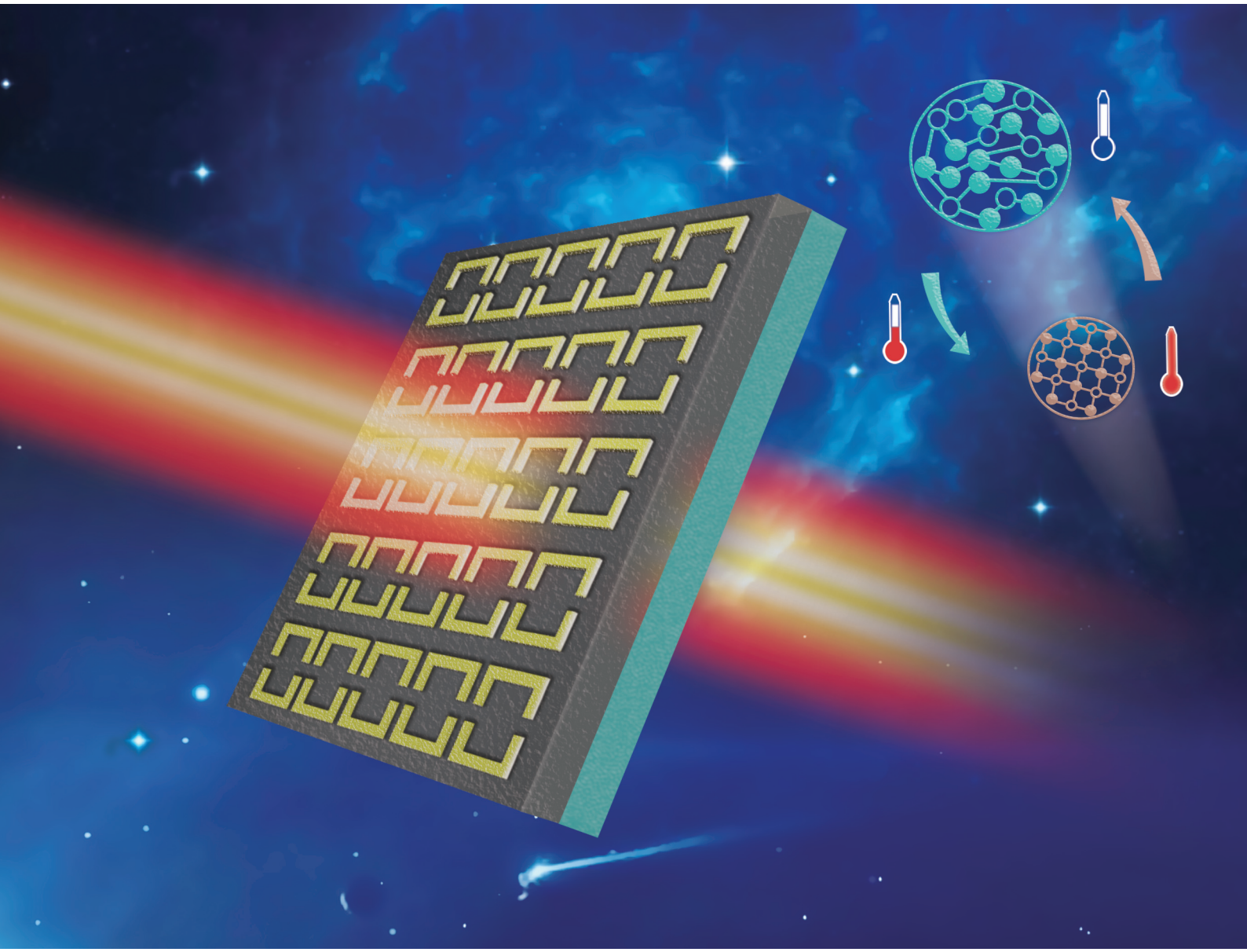

ISSN 2040-3372

ROYAL SOCIETY OF CHEMISTRY

PAPER

Fuli Zhang, Changzhi Gu, Junjie Li *et al.*
Realization of a near-infrared active Fano-resonant asymmetric metasurface by precisely controlling the phase transition of $Ge_2Sb_2Te_5$

NCNST

Nanoscale

ROYAL SOCIETY OF CHEMISTRY

PAPER

View Article Online
View Journal | View Issue

Cite this: *Nanoscale*, 2020, **12**, 8758

Realization of a near-infrared active Fano-resonant asymmetric metasurface by precisely controlling the phase transition of $Ge_2Sb_2Te_5$†

Wei Zhu, ‡[a,b] Yuancheng Fan, ‡[b] Ce Li,[a,c] Ruisheng Yang,[b] Shi Yan,[a] Quanhong Fu,[b] Fuli Zhang, *[b] Changzhi Gu*[a,c] and Junjie Li *[a,c,d]

Received 20th November 2019,
Accepted 8th February 2020

DOI: 10.1039/c9nr09889e

rsc.li/nanoscale

A metasurface is one of the most effectual platforms for the manipulation of complex optical fields. One of the current challenges in the field is to develop active or reconfigurable functionalities to extend its operation band which is limited by its intrinsic resonant nature. Here we demonstrate a kind of active Fano-resonant asymmetric metasurface in the near-infrared (NIR) region with heterostructures made of a layer of asymmetric split-ring resonators and a thin layer of phase-change material (PCM). In the asymmetric metasurface, significant tunability in the frequency, *Q*-factor and strength of the Fano resonance are all achieved by precisely controlling the phase transition of the contained PCM $Ge_2Sb_2Te_5$ (GST), together with changing the geometric asymmetry of the split-ring resonators. Moreover, we provide a complete transition process of the optical properties for GST and an optimized modulation on the active Fano-resonant metasurface. Our approach to dynamically control a Fano-resonant metasurface paves the way to realizing various active photonic meta-devices involving PCM.

Introduction

A metasurface, a kind of metamaterial[1–7] made of few functional layers, has been intensively investigated as a powerful tool for manipulating complex optical fields. The optical properties of metasurfaces can be arbitrarily tailored by rationally designing their building blocks or meta-atoms for exotic light manipulations including orbital angular momentum (OAM),[8,9] meta-holography[10,11] and harmonic signal generation.[12–14] Compared with three-dimensional (3D) metamaterials, the fabrication of two-dimensional (2D) metasurfaces is much easier especially in optical frequencies. Metasurfaces are usually composed of various metallic resonators operating with properly designed resonant modes. When the operating frequency goes to the optical regime, the resonant properties *i.e.* the *Q*-factors of metasurfaces are always limited by the Drude damping of most of the plasmonic materials that restrict their practical applications. There have been reports of various meta-devices with low-loss materials *e.g.* silver, aluminum,[15–17] and all-dielectrics.[18–26] Apart from that, high-*Q* line-shaped resonances can also be obtained by geometric tailoring[27] or by breaking the symmetry of the structure in plasmonic metasurfaces.[28–30] Fano[31] resonance was firstly found in quantum systems with an unusual asymmetric line-shape instead of a symmetric Lorentzian profile. The strong dispersion characteristics of Fano or electromagnetically induced transparency (EIT) line-shapes in photonics[32,33] which can supply sharp transmission–reflection curves could overcome the drawbacks. It has been demonstrated that Fano resonances have broad application prospects in biomedicine[34] and SERS sensors.[35]

In view of the practical applications of resonant metasurfaces, it is highly desirable to achieve a high-*Q* response with an extended operation frequency band by incorporating functional materials which are sensitive to external stimuli, such as carbon nanotubes,[35] liquid crystals,[36,37] graphene[38–42] transition metal dichalcogenides (TMDCs)[43,44] *etc*. Among these, the phase change material (PCM) $Ge_2Sb_2Te_5$ (GST)[45] is extremely scalable, non-volatile, and easily integrated in commercial devices[46,47] which means it holds great potential in appli-

[a]*Beijing National Laboratory for Condensed Matter physics, Institute of Physics, Chinese Academy of Sciences, Beijing 100190, China. E-mail: jjli@iphy.ac.cn, czgu@iphy.ac.cn*
[b]*School of Physical Science and Technology and Shenzhen Research & Development Institute, Northwestern Polytechnical University, Xi'an 710129, China. E-mail: fuli.zhang@nwpu.edu.cn*
[c]*School of Physical Sciences, CAS Key Laboratory of Vacuum Physics, University of Chinese Academy of Sciences, Beijing, 100049, China*
[d]*Songshan Lake Materials Laboratory, Dongguan, Guangdong, 523808, China*
†Electronic supplementary information (ESI) available. See DOI: 10.1039/c9nr09889e
‡These authors contributed equally to this work.

cations such as data storage,[48] solid-state, flexible displays[46] and algorithm processing.[49] The optical properties of GST can be drastically changed during phase changing from amorphous (a-GST) to the crystalline state (c-GST) by applying external stimuli such as heat,[50] photon,[51,52] or electric energy.[53–55] More interestingly, GST has both stable phases at room temperature and can be switched quickly and reversibly between one and the other without volatilization at a time scale of 50 ns.[56] Based on these excellent features, it has been experimentally demonstrated with impressive modulation capabilities in thermal emission;[57–61] optical switches,[56,62] electromagnetic absorption[63] and non-radiation mode.[64] However, experimental studies have mainly focused on the switching/modulation of GST based meta-devices considering the initial and final states of the phase transition considering the dramatic differences of the optical constants between the two states. The arbitrary state during the phase transition with a controllable ratio of amorphous and crystalline components has also been theoretically studied for EIT,[65] polarization conversion,[66] toroidal[67] and beam deflectors.[68] It is worthy of note that GST can be stable in an arbitrary intermediate state between a-GST and c-GST by precisely controlling the energy and duration of the external stimulus. Therefore, metasurfaces based multifunctional photonics devices can be realized by precisely controlling the phase transition level of the incorporated GST medium.

In this article, we demonstrate an active Fano-resonant metasurface with dynamically tunable resonant frequencies by precisely controlling the phase transition of the GST nanofilm. The studied Fano-resonant metasurface is made of a thin layer of GST and a top layer with structured resonators. For simplicity and without loss of generality, the classical asymmetric split-ring resonator (ASRR) array was employed for the Fano-resonant structure. By precisely controlling the phase transition process, we experimentally demonstrated that the Fano resonance (including the resonant frequency, resonant strength and Q-factor) can be continuously tuned under *in situ* baking. Moreover, we studied the relationship between baking temperature and the crystallization ratio by *in situ* XRD in the process of baking. In this way, the arbitrary crystallization ratio of crystallization GST between a-GST and c-GST can be obtained by controlling the temperature of baking. Simultaneously, combined with the changes of the asymmetry geometric parameter of the ASRRs, we investigated the changed laws of the Q-factor of Fano lineshapes. The metasurface with the phase transition process of GST demonstrated here paves an alternative method to realize a dynamically tunable high-Q Fano resonance metasurface as well as other functional meta-devices.

Materials and design

The designed structure is schematically illustrated in Fig. 1. The active tunable metasurface is able to realize the continuous manipulation of the Fano resonance by precisely controlling the phase state of the functional layer GST. We choose the *in situ* baking as the external stimulus to control the GST crystallization ratio. The proposed metasurface is composed of fused silica, functional GST film, silica cap and ASRRs, as shown in Fig. 1b. The three-layer structures are deposited on a fused silica substrate with a refractive index n = 1.46. The periodicity of the ASRRs is p = 700 nm, and the length and width of resonators are $p_x = p_y$ = 330 nm. The gap and width of the resonators are g = 90 nm and w = 60 nm, respectively. The parameter Δ represents the distance between the center of the gap and the center of ASRRs along the x-axis, which determines the asymmetric degree. A 50 nm thick gold ASRRs is on the top of structure, followed by a 40 nm thick SiO_2 spacer layer which separates the Au resonators from the 20 nm functional layer GST. The spacer layer plays the vital role since it can protect the GST film from oxidation during the process of phase transition and at the same time, preventing the gold and GST materials from interdiffusing during baking. To facilitate the design of the metasurface, we employed a commercial full-wave simulation software CST Microwave Studio based on the finite integration method to calculate the optical responses of the proposed metasurface. In simulation, unit cell boundary conditions are applied to the x- and y-axis to simulate an infinite periodic array, the simulated results are obtained at normal incidence. The electric field E, the magnetic field H and the wave vector k are in the x, y and z directions, respectively. The permittivity of Au is described by the Drude model: $\varepsilon(\omega) = 1 - \omega_p^2/(\omega^2 + i\gamma\omega)$, where $\omega_p = 1.37 \times 10^{16}$ rad s^{-1} is the plasma frequency and $\gamma = n \times 4.08 \times 10^{13}$ rad s^{-1} is the damping rate (n = 2). The relative permittivity of a-GST and c-GST (0.2–2.5 μm) used in our simulation is measured by an ellipsometer with a sample of 20 nm GST thin film deposited on the fused silica substrate.

At first, we systematically studied the phase transition process and the intermediate states of the PCM GST using X-ray diffraction characterization and ellipsometry measurements under *in situ* baking. It is worth noting that the crystallized GST has a face-centered cubic phase (FCC) and a hexagonal phase (HEX) with two different atomic arrangements. Although the crystallization temperature of GST has been studied previously in some works,[56,60] we here confirm the crystallization temperature of GST through X-ray diffraction (XRD) in order to eliminate the experimental deviation from thickness, fabricated methods or some other factors of the thin film. Fig. 2c shows the XRD patterns of the baked 20 nm GST thin film by the grazing incidence of the X-rays. After baking at 150 °C, the GST thin film exhibited a partially crystalline state, with diffraction peaks near 28°, which indicates the appearance of FCC-GST. With the further increase of the baking temperature, the diffraction peaks near 26° and 38° prove that a majority of FCC-GST have transformed to HEX-GST when the baking temperature reaches 250 °C. It can be observed that the characteristic peak of HEX-GST is beginning to appear at 210 °C, which does not exist at 180 °C. In other words, GST has realized the crystallization from amorphous to the FCC phase completely between 180 °C to 210 °C.

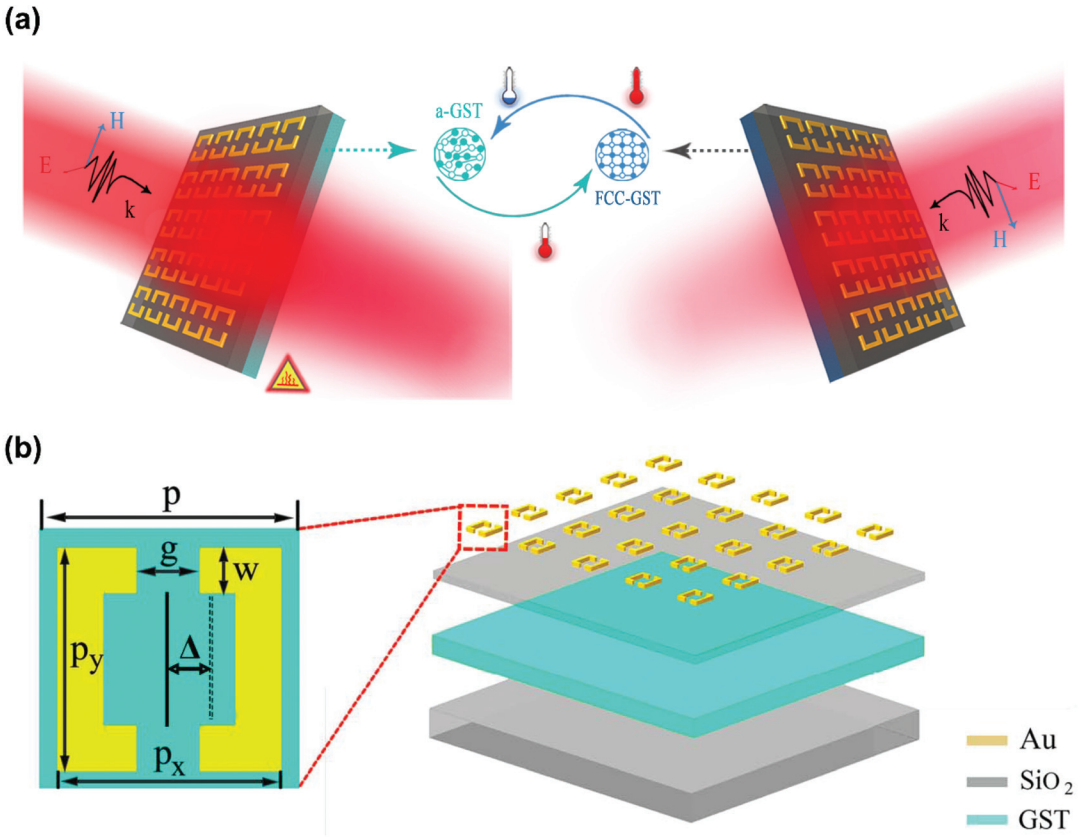

Fig. 1 Schematic of the precisely continuously tunable Fano resonanant metasurface. (a) Schematic illustration of the working mechanism of the metasurface. Fano resonance is obtained by breaking the symmetry of the structure. The lineshape of the Fano resonance can be controlled precisely *via in situ* baking of the functional layer GST. (b) The schematic of the composition and the unit cell of the metasurface.

Combining the results of transmission electron microscopy (TEM) with the sample baked at 180 °C shown in Fig. 2d, we are able to further confirm that the GST functional layer is nearly in the FCC state with a 180 °C–210 °C baking temperature. It is clearly shown that in almost all areas stripes have appeared, which means that the functional GST layer has been crystallized. At the same time, the selected area electron diffraction (SAED) in the inset has also indicated the GST is nearly complete crystallized. Furthermore, we are able to prove the GST is FCC instead of HEX by observing the arrangement of atoms (see section S1, ESI†).

The optical constants of the PCM GST measured by the ellipsometer are shown in Fig. 2a where lines and solid lines with dots represent the a-GST and the c-GST, respectively. The difference of the real part of permittivity between the amorphous and crystallized states will be more obvious with the wavelength longer than 700 nm. The imaginary part of the permittivity is very small when GST is in amorphous phase, and the imaginary part increases dramatically during the phase transition process. In the designing of the metasurface, we choose the parameters to make sure the fundamental plasma resonance is located in the transparency window of GST, that is, between 1.2 and 2.5 μm for both the amorphous and the crystalline phase where absorption losses of such a thin film are negligibly small. The optical constants of GST with an arbitrary hybridization ratio of a-GST and c-GST are presented in Fig. 2b which were calculated using the Lorenz–Lorentz relations:[69]

$$\frac{\varepsilon_{\mathrm{eff}}(\lambda)-1}{\varepsilon_{\mathrm{eff}}(\lambda)+2} = m \times \frac{\varepsilon_{\mathrm{c}}\text{-GST}(\lambda)-1}{\varepsilon_{\mathrm{c}}\text{-GST}(\lambda)+2} + (1-m) \times \frac{\varepsilon_{\mathrm{a}}\text{-GST}(\lambda)-1}{\varepsilon_{\mathrm{a}}\text{-GST}(\lambda)+2} \quad (1)$$

where ε_{c}-GST(λ) and ε_{a}-GST(λ) are the wavelength-dependent dielectric constants of GST in the crystalline and amorphous states, and m is the crystallization fraction of GST ranging from 0 (pure a-GST) to 1 (pure c-GST). Note that we just define the permittivity of FCC-GST as ε_{c}-GST, because the loss of HEX-GST is too high to transmit a signal. As shown in Fig. 2b, the permittivity of several intermediate states of GST has also been calculated. It is clear that the real parts of the permittivity of different intermediate states GST have obvious disparities while the imaginary part of permittivity stays low, which can ensure the functional layer of GST to maintain high modulation efficiency during phase transition.

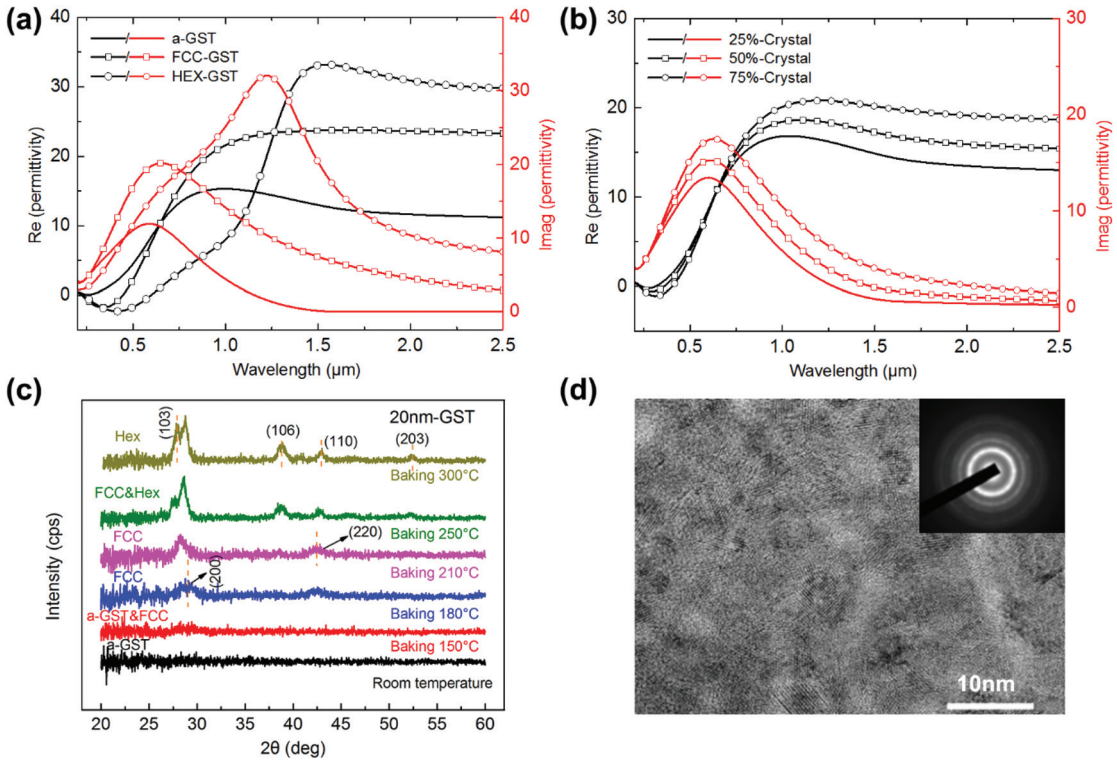

Fig. 2 The properties of the GST functional layer. (a) The permittivity of the a-GST, FCC-GST and HEX-GST measured by an ellipsometer. (b) The permittivity of the 25%-crystal GST, 50%-crystal GST and 75%-crystal GST were calculated through Lorenz–Lorentz relations. (c) The XRD data were measured with a 20 nm GST layer after *in situ* baking by baking accessories. (d) The TEM image of the 20 nm GST layer after 180 °C baking. Inset: The SAED of the sample.

Results and discussion

Fig. 3a shows the samples with five different asymmetry parameters, which are defined as $\eta = \dfrac{\Delta}{\dfrac{p_x}{2} - w - \dfrac{g}{2}} \times 100\%$, where p_x, w, g and Δ have been defined in Fig. 1b. So, the asymmetry parameter can be simply expressed as $\eta = \dfrac{\Delta}{60} \times 100\%$. The samples are addressed as ASRR1 to ASRR5 with from η = 0% to η = 100% with a fixed step of 25%, and the corresponding scanning electron microscope (SEM) images of ASRRs are given. For ASRR1, which possesses mirror symmetry along the x- and y-axis, an electric dipolar resonance dominates as the incident electric field is oriented along the y-axis at normal incidence. When structural symmetry breaking is introduced into the unit cell of the metasurface, an additional Fano resonance appears at lower frequencies and its resonant frequency shows a red shift with the increase of the degree of asymmetry (Fig. 3b). Compared to the electric dipolar resonances, this additional resonance, or so-called "trapped mode", is more sharp due to the fact that the mode is weakly coupled to free space.[70] The high-Q Fano line-shape of the resonance originates from the interference of the "trapped mode" and the background polarization.[32,71] It is worth noting that the high-Q of the Fano resonance can also be understood as a result of the distortion of symmetry-protected bounded states in the continuum,[72] the structural symmetry breaking brings the bound states in continuum (BIC) into a quasi-BIC which is weakly coupled to free space and of high-Q. It is easy to ascertain that the strength of the Fano mode resonance [$(T_{max} - T_{min}) \times 100\%$] will be stronger with the increase of the asymmetry parameter. It is noted that with the increase of the thickness of the functional layer of GST, the modulation effects will become more and more obvious. However, too thick a GST layer will cause a decrease in transmittance. The same is true of the thickness of the cap layer: too thin a cap layer is not able to prevent oxidation of the GST layer while too thick a cap layer will affect the effect of modulation.

There are several ways to expound the coupling mechanisms between the resonators such as coupled mode theory,[73] equivalent circuit modeling[74] or the coupled oscillator model.[75] In this work, we use the coupled oscillator model in which the bright mode is the coupled dipole resonance regarded as the continuum and the dark mode is the leaky mode to theoretically explain the continuous Fano resonance. The interaction of the bright and dark modes in the coupled system can be described as:

$$\ddot{x}_b + \gamma_b \dot{x}_b + {\omega_b}^2 x_b + \kappa x_d = gE \quad (2)$$

$$\ddot{x}_d + \gamma_d \dot{x}_d + {\omega_d}^2 x_d + \kappa x_b = 0 \quad (3)$$

where (x_b, x_d), (γ_b, γ_d), and (ω_b, ω_d) are the amplitudes, damping rates and the resonance frequencies of the bright and the dark modes, κ is the coupling coefficient between the bright mode and dark mode, and g is the geometric parameter which shows the

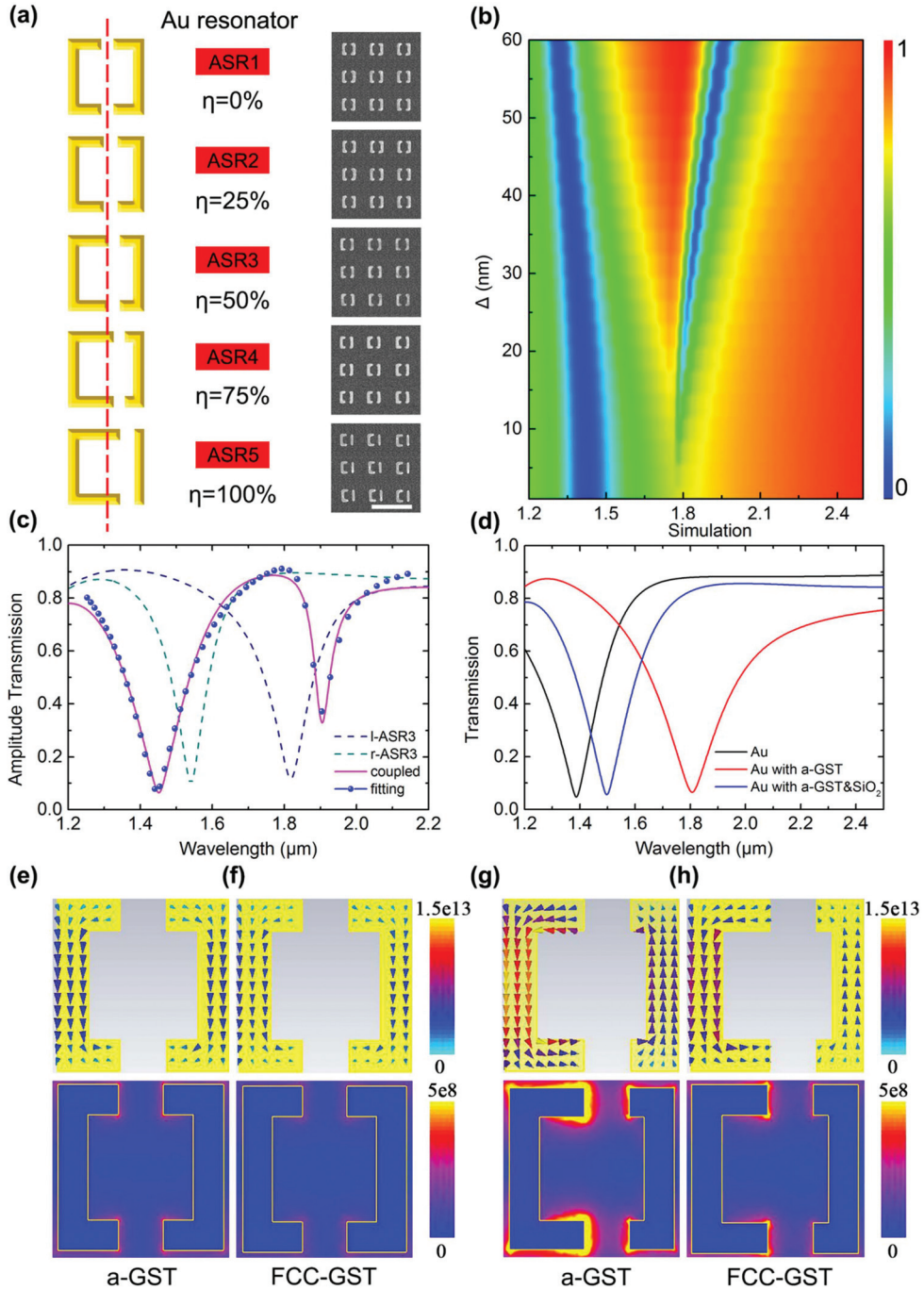

Fig. 3 The properties of the metasurface with different ASRs. (a) The SEM images of five different samples which can realize the precisely continuously controllable Fano resonance metasurfaces (scale bar: 1 μm). (b) The relationship between the Fano mode resonance and degree of asymmetry. (c) Simulated amplitude transmission spectra of individual arms and the coupled SRR system while η = 50%. (d) Relationship between dipole mode resonance and dielectric environment. (e and f) Surface current distribution and *E*-field pattern of the dipole resonance of ASRR1 with a-GST and FCC-GST. (g and h) Surface current distribution and *E*-field pattern of the Fano resonance of ASRR3 with a-GST and FCC-GST.

coupling strength of the bright mode with the incident field *E*. By solving x_b and x_d, the susceptibility expression can be given:

$$\chi = g\left(\frac{(\omega^2 - {\omega_d}^2) + i\omega\gamma_d}{\kappa^2 - (\omega^2 - {\omega_b}^2 + i\omega\gamma_b)(\omega^2 - {\omega_d}^2 + i\omega\gamma_d)}\right) \quad (4)$$

Here, Re[χ] and Im[χ] represent the dispersion and the absorption (loss) within the medium, respectively. According to the conservation of the energy relation $T + A = 1$, the transmission coefficient is defined as $T = 1 - A$ (given by the Kramer–Kronig relations) where A = Im[χ] is the absorption/losses in the medium. We neglect other nonresonant scattering losses because they do not show any effect on the experiment and simulation. Fig. 3c depicts the fitting curve of ASRR3 which exhibits an excellent agreement with the simu-

lated curves and the plot parameters $\omega_b = 1.28 \times 10^{15}$ rad s^{-1}, $\omega_d = 1.03 \times 10^{15}$ rad s^{-1}, $\gamma_b = 2.32 \times 10^{14}$ rad s^{-1}, $\gamma_d = 2.66 \times 10^{13}$ rad s^{-1}, $\kappa = 2.22 \times 10^{17}$ rad^2 s^{-2} and $g = 2.63 \times 10^5$ are extracted from the simulated curves. The dissipation factor of the bright mode γ_b is nearly ten times larger than γ_d, which gives rise to the narrow transparent windows. The strength of the Fano resonance depends on the coupling coefficient κ which relates to the asymmetry parameter η. The dashed lines represent the separate individual arms of the ASRR3, where the dips of transmission spectra are in different frequencies because of the different arm lengths. The asymmetric resonant behavior can be controlled by adjusting the interference between a broad continuum and a discrete resonant scattering process, which are attributed to the constructive or destructive interference between a low *Q*-factor bright mode and a narrow distinctive dark mode through breaking the structure symmetry. Fig. 3d shows the simulated results with a different dielectric layer of metasurface which consists of symmetric double split-ring resonators. With the introduction of the GST layer and the cap layer between the substrate and resonators, the dip of the resonance shifts significantly. According to the equivalent LC circuit model, we have explained this blue-shift phenomenon with the increase of the thickness of cap layer, which is mainly attributed to the engineering of the dielectric environment of the parallel plate capacitance.[63] To further reveal the mechanism of the Fano resonance, we study the *E*-fields and distribution of surface current of the resonators. Fig. 3e and f show the distribution of the surface current and *E*-field of ASRR1 when the functional layers are a-GST and FCC-GST. The current on two individual arms is in the same direction, which shows they couple with the external *E*-field. The two arms of ASRR1 induce electric fields with an equivalent magnitude under the excitation of incident light. There is no doubt that it has no contribution to suppress the radiation loss so that the capacity of confining the *E*-field of resonators is weak. Compared to the dipolar resonance mode, the Fano resonance mode has a much stronger confinement of the electric field in the capacitive split gaps of the asymmetric resonators, as shown in Fig. 3h. At the same time, different from the dipolar resonance mode which is more likely two independent resonances from two equivalent arms of the resonator, the Fano resonance mode can be attributed to the magnetic coupling of the resonator due to the antiparallel surface currents of the two unequal adjacent arms forming a closed loop, which is shown in Fig. 3g. Since the structure only weakly couples to the free space, the current is very pronounced. In addition, the most important thing is that the leakage current which represents the magnitude of the surface currents in the two arms is different. The stronger leakage current which is caused by the increase in asymmetry leads to reduced values of the *Q*-factor ($Q = f_0/\Delta f$) which is the ratio of the resonance frequency and the full width at half maxima of the Fano resonance by broadening the resonance due to the higher radiative losses and stronger coupling to free space.

We have investigated the characteristics of the Fano metasurface with different asymmetry degrees when the functional layer GST is amorphous and crystalline, respectively, as shown in Fig. 4a–d. The dipolar resonance appears at 1.5 μm when the resonators are symmetrical along *y*-axis. We observe the additional Fano resonance mode once the symmetry of the structure is broken. By optimizing the sizes of the resonator and the thickness of the spacer layer, the dips of the Fano resonances lie exactly in the area where the optical constants of GST possess the most significant change from amorphous to crystallization. We observe that the *Q*-factor and the strength of Fano resonance varies with η obviously. We deliberately increase the degree of asymmetry in order to explore the law of change of the *Q*-factor and the strength of the resonance. As shown in the Fig. 4e–h, the *Q*-factor and the resonance

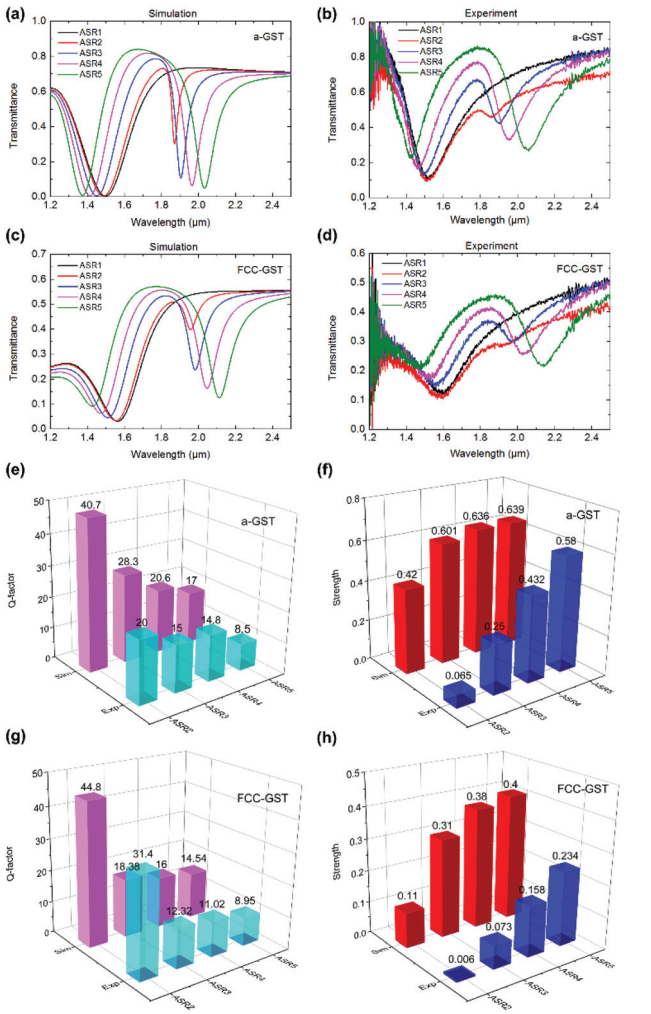

Fig. 4 The properties of the Fano resonance mode with a-GST and FCC-GST. (a and b) The simulated and corresponding experimental transmittance spectra with different degrees of asymmetry of structure when GST is amorphous. (c and d) The simulated and corresponding experimental transmittance with different degrees of asymmetry of structure when GST is FCC-GST. (e and f) *Q*-Factor and strength of Fano resonance varying with the degree of asymmetry of structure when GST is amorphous. (g and h) *Q*-Factor and strength of Fano resonance varied with the degree of asymmetry of structure when GST is FCC-GST.

strength show the opposite trends with the increase of the asymmetry, a trade-off must be made between them.[76] From ASRR2 to ASRR5, the simulated strength of resonances increases from 0.42 to 0.64 with the cost of the *Q*-factor dropping from 47.9 to 17, while the corresponding experimental values are from 0.065 to 0.58 and 20 to 8.5 when GST is in the amorphous state. Compared with the a-GST, the strength of Fano resonance will be significantly reduced due to the large absorption of c-GST, as shown in Fig. 4h. On the contrary, the *Q*-factor of the Fano resonance in Fig. 4g only has slightly changed with Fig. 4e owing to the stable leakage current which is mainly influenced by the asymmetry parameter instead of the dielectric environment. Interestingly, since the weak coupling intensity of the bright mode and dark mode varied by the degree of asymmetry, the separated wavelength distance between the dipolar resonance mode and Fano resonance mode becomes larger and larger with the difference in the length of the two arms of the ASRRs.[77] The degree of asymmetry determines the intensity of leakage current which directly influences the *Q*-factor and the strength of the Fano resonance. Furthermore, in order to better verify the potential of our design, we have also separately studied the effects of the thickness of the GST layer and the cap layer on the resonances (see section S2, ESI†).

A continuously controllable Fano metasurface at normal incidence has been demonstrated in simulations and experiments, as shown in Fig. 5a and b. With the increase of crystallization ratio, the dip of Fano resonance will redshift from 1.91 μm to 1.99 μm. Simultaneously, we have realized the manipulation of *Q*-factor and strength of Fano resonance without changing the asymmetry of the resonators. In order to verify the manipulation of Fano resonance derived by the phase transition of the GST functional layer, the continuously controllable metasurface is baked at 5 °C steps from 120 °C to 235 °C to get different intermediate phases of GST. In the process of the phase transition, we have found the exact temperature with different crystallization ratios. The measured transmittance spectra are in good agreement with the simulated transmittance spectra. As shown in Fig. 5c and d, both the *Q*-factor and the strength of Fano resonances decrease with the increase of the crystallization ratio, which do not follow the inverse relationship between the *Q*-factor and the strength of resonance. This phenomenon can be explained by the fact that the extinction coefficient which determines the loss of material will increase with the process of phase transition. Note that we can guarantee that the baking temperature has an absolutely precise relationship with the degree of GST phase transition although the baking temperature is not the only factor that influences the phase transition, which is also affected by the baking time. In experiment, we make the *in situ* baking device heat up with steps of 5 °C and stay for 3 minutes to collect the spectrum of transmittance. In this way, the influence which is induced by the baking time can be negligible. We only display the results of ASRR3 with asymmetric parameter η = 50%, the other results with different asymmetry parameters have also been investigated (see section S3, ESI†). Moreover, we also investigate the change of Fano resonance performances with the functional layer GST from FCC to HEX (see section S4, ESI†).

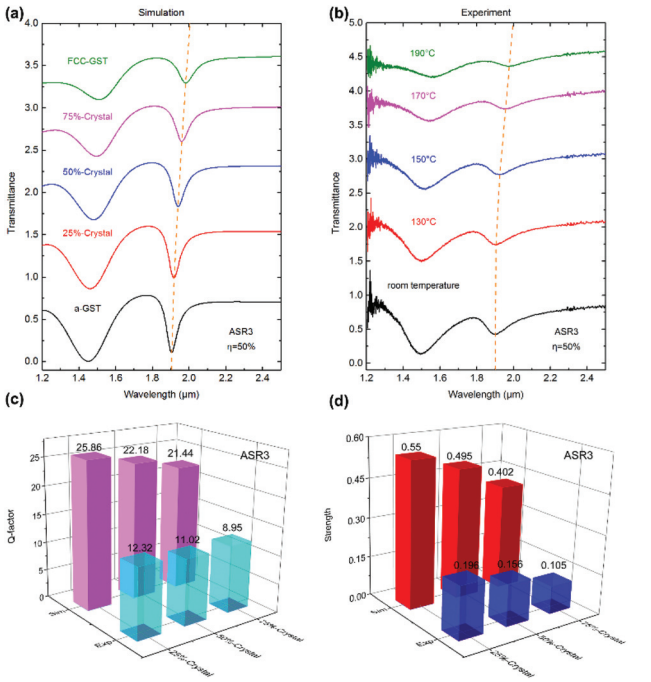

Fig. 5 The properties of the Fano resonance mode with different crystalline ratios. (a) The simulated transmittance with different crystalline ratios. (b) The corresponding experimental transmittance with different *in situ* baking temperatures. (c and d) The *Q*-factor and strength of resonance with different degrees of crystallization.

Meanwhile, the repeated cycles which represent GST from crystallization to amorphous should be taken into account. Some other methods that can realize the reamorphization of GST have been proposed, because the annealing temperature should be above 640 °C followed by a sharp cooling while we observed that Au film undergoes obvious deformation around 300 °C. In addition to annealing, the reamorphization of GST can be realized by electrical stimuli with several nanoseconds and laser pluses with femtoseconds.[56,78]

Conclusions

In conclusion, we have demonstrated ultrathin continuously controllable Fano resonance and NIR transmission modulation characteristics of a metasurface device comprising a plasmonic ASRR array hybridized with a phase change layer of GST as an active medium. Taking advantage of the features of GST, we have realized the arbitrary intermediate states of GST in the process of phase transition (from amorphous to FCC or even to HEX) by *in situ* baking. We have systematically studied the relationship between baking temperature and the crystallization ratio by *in situ* XRD in the process of baking gradually. In this way, an arbitrary crystallization ratio between a-GST

and c-GST can be obtained by controlling the temperature of baking. Compared to the conventional way of modulating Fano resonance by changing the structural symmetry, our approach provides a new degree of freedom for it. There is no doubt that the ultrathin continuously controllable Fano resonance metasurface will benefit plenty of applications such as biomolecular detection and SERS sensors.

Methods

Sample fabrications

In this work, a fused silica wafer with a thickness of 500 μm was used as the substrate. Prior to deposition, the silica substrates were cleaned ultrasonically in acetone, isopropanol and deionized water, and finally dried with nitrogen. Then, a 20 nm GST thin film was first deposited onto the fused silica substrate by an ultra-high vacuum ion beam laser pulse deposition system (Combo-1220). The sputtering pressure was 0.007 Torr, and the chamber base pressure was 6×10^{-7} Torr. The GST target diameter was 50.8 mm and its purity was 99.9%. GST was sputtered using a power of 100 W at a radiofrequency (RF) gun with 1 Å s^{-1}. The cap layer, about 40 nm, of SiO_2 was deposited by a plasma enhanced chemical vapor deposition system (PECVD) (System100 PECVD System) with a deposition rate of 5 Å s^{-1}. Then, 200 nm thick positive resist layer polymethyl methacrylate (PMMA) was spin-coated onto the SiO_2/GST layers. Note that the baking temperature of the electron resist was 383 K for 30 min to prevent the undersigned phase transition of GST. Subsequently, the PMMA resist was exposed by electron-beam lithography (JBX-6300FS) and thus the nanopatterns were formed. After developing, the electron-beam evaporation method was used to deposit a 50 nm Au film on the sample. At last, the nano-resonators were formed after a lift-off process of soaking the sample in acetone.

Sample measurements

The results of the XRD were measured by a high-resolution X-ray diffractometer (SmartLab). We adopt the grazing incidence to characterize the sample due to the thin GST film. A different ratio of crystalline GST was obtained by baking with *in situ* baking accessories. The optical constants of GST were measured by an ellipsometer (SE 850 DUV). The transmittances spectra were measured by an FTIR spectrometer (Vortex 70v) coupled to a Bruker IR microscope (Hyperion 2000). The setup was capable of collecting data over the NIR (8400–3800 cm^{-1}) region with a spectral resolution of 1 cm^{-1}. All spectroscopic data were collected in transmission mode by a potassium bromide (KBr) beam splitter. The scanner velocity was set to be 20 kHz. We have added an *in situ* baking accessory in the micro-zone under the microscope. The distance between the baking accessory and microscope was above 3 cm which can ensure the microscope works properly. We set the baking range from 120 °C to 235 °C in steps of 5 °C. Spectral data were acquired with OPUS 6.0 software.

Conflicts of interest

There are no conflicts to declare.

Acknowledgements

The authors acknowledge the financial support received from the National Key R&D Program of China (Grant No. 2016YFA0200800 and 2016YFA0200400), the National Natural Science Foundation of China (Grant No. 11674387, 11574369, 91323304, 11574368, 11574385, 61771402, 11674266 and 61888102), the Key Research Program of Frontier Sciences of CAS (Grant No. QYZDJ-SSW-SLH042), and the Shenzhen Science and Technology Innovation Commission (JCYJ20170817162221169).

Notes and references

1 D. R. Smith, J. B. Pendry and M. C. Wiltshire, *Science*, 2004, **305**, 788–792.
2 R. Gordon, A. G. Brolo, D. Sinton and K. L. Kavanagh, *Laser Photonics Rev.*, 2010, **4**, 311–335.
3 T. W. Ebbesen, H. J. Lezec, H. Ghaemi, T. Thio and P. Wolff, *Nature*, 1998, **391**, 667.
4 J. Valentine, S. Zhang, T. Zentgraf, E. Ulin-Avila, D. A. Genov, G. Bartal and X. Zhang, *Nature*, 2008, **455**, 376.
5 V. M. Shalaev, *Nat. Photonics*, 2007, **1**, 41.
6 N. I. Landy, S. Sajuyigbe, J. J. Mock, D. R. Smith and W. J. Padilla, *Phys. Rev. Lett.*, 2008, **100**, 207402.
7 S. Zhang, D. A. Genov, Y. Wang, M. Liu and X. Zhang, *Phys. Rev. Lett.*, 2008, **101**, 047401.
8 M. I. Shalaev, J. Sun, A. Tsukernik, A. Pandey, K. Nikolskiy and N. M. Litchinitser, *Nano Lett.*, 2015, **15**, 6261–6266.
9 G. Li, M. Kang, S. Chen, S. Zhang, E. Y.-B. Pun, K. W. Cheah and J. Li, *Nano Lett.*, 2013, **13**, 4148–4151.
10 L. Huang, X. Chen, H. Mühlenbernd, H. Zhang, S. Chen, B. Bai, Q. Tan, G. Jin, K.-W. Cheah and C.-W. Qiu, *Nat. Commun.*, 2013, **4**, 2808.
11 W. Ye, F. Zeuner, X. Li, B. Reineke, S. He, C.-W. Qiu, J. Liu, Y. Wang, S. Zhang and T. Zentgraf, *Nat. Commun.*, 2016, **7**, 11930.
12 M. W. Klein, C. Enkrich, M. Wegener and S. Linden, *Science*, 2006, **313**, 502–504.
13 N. Segal, S. Keren-Zur, N. Hendler and T. Ellenbogen, *Nat. Photonics*, 2015, **9**, 180.
14 M. Ren, B. Jia, J. Y. Ou, E. Plum, J. Zhang, K. F. MacDonald, A. E. Nikolaenko, J. Xu, M. Gu and N. I. Zheludev, *Adv. Mater.*, 2011, **23**, 5540–5544.
15 P. R. West, S. Ishii, G. V. Naik, N. K. Emani, V. M. Shalaev, and A. Boltasseva, *Laser Photonics Rev.*, 2010, **4**, 795–808.
16 B. Wild, L. Cao, Y. Sun, B. P. Khanal, E. R. Zubarev, S. K. Gray, N. F. Scherer and M. Pelton, *ACS Nano*, 2012, **6**, 472–482.

17 Y. Zhang, Z. Ouyang, N. Stokes, B. Jia, Z. Shi and M. Gu, *Appl. Phys. Lett.*, 2012, **100**, 151101.
18 C. Wu, N. Arju, G. Kelp, J. A. Fan, J. Dominguez, E. Gonzales, E. Tutuc, I. Brener and G. Shvets, *Nat. Commun.*, 2014, **5**, 3892.
19 H. Liu, C. Guo, G. Vampa, J. L. Zhang, T. Sarmiento, M. Xiao, P. H. Bucksbaum, J. Vučković, S. Fan and D. A. Reis, *Nat. Phys.*, 2018, **14**, 1006.
20 Y. Yang, I. I. Kravchenko, D. P. Briggs and J. Valentine, *Nat. Commun.*, 2014, **5**, 5753.
21 Y. F. Yu, A. Y. Zhu, R. Paniagua-Domínguez, Y. H. Fu, B. Luk'yanchuk and A. I. Kuznetsov, *Laser Photonics Rev.*, 2015, **9**, 412–418.
22 Y. Yang, W. Wang, P. Moitra, I. I. Kravchenko, D. P. Briggs and J. Valentine, *Nano Lett.*, 2014, **14**, 1394–1399.
23 K. E. Chong, I. Staude, A. James, J. Dominguez, S. Liu, S. Campione, G. S. Subramania, T. S. Luk, M. Decker and D. N. Neshev, *Nano Lett.*, 2015, **15**, 5369–5374.
24 M. Khorasaninejad, W. T. Chen, R. C. Devlin, J. Oh, A. Y. Zhu and F. Capasso, *Science*, 2016, **352**, 1190–1194.
25 A. Amir, H. Yu, B. Mahmood and F. Andrei, *Nat. Nanotechnol.*, 2015, **10**, 937–943.
26 S. Wang, P. C. Wu, V. C. Su, Y. C. Lai, M. K. Chen, H. Y. Kuo, H. C. Bo, H. C. Yu, T. T. Huang and J. H. Wang, *Nat. Nanotechnol.*, 2018, **13**, 227–232.
27 D. O. Guney, T. Koschny and C. M. Soukoulis, *Phys. Rev. B: Condens. Matter Mater. Phys.*, 2010, **80**, 125129.
28 M. Manjappa, Y. K. Srivastava, L. Cong, I. Al-Naib and R. Singh, *Adv. Mater.*, 2017, **29**, 1603355.
29 L. Cong, M. Manjappa, N. Xu, I. Al-Naib, W. Zhang and R. Singh, *Adv. Opt. Mater.*, 2015, **3**, 1537–1543.
30 V. Fedotov, M. Rose, S. Prosvirnin, N. Papasimakis and N. Zheludev, *Phys. Rev. Lett.*, 2007, **99**, 147401.
31 U. Fano, *Phys. Rev.*, 1961, **124**, 1866.
32 A. E. Miroshnichenko, S. Flach and Y. S. Kivshar, *Rev. Mod. Phys.*, 2010, **82**, 2257.
33 M. F. Limonov, M. V. Rybin, A. N. Poddubny and Y. S. Kivshar, *Nat. Photonics*, 2017, **11**, 543.
34 C. Wu, A. B. Khanikaev, R. Adato, N. Arju, A. A. Yanik, H. Altug and G. Shvets, *Nat. Mater.*, 2012, **11**, 69.
35 A. E. Nikolaenko, F. De Angelis, S. A. Boden, N. Papasimakis, P. Ashburn, E. Di Fabrizio and N. I. Zheludev, *Phys. Rev. Lett.*, 2010, **104**, 153902.
36 X. Wang, D.-H. Kwon, D. H. Werner, I.-C. Khoo, A. V. Kildishev and V. M. Shalaev, *Appl. Phys. Lett.*, 2007, **91**, 143122.
37 B. Kang, J. Woo, E. Choi, H.-H. Lee, E. Kim, J. Kim, T.-J. Hwang, Y.-S. Park, D. Kim and J. Wu, *Opt. Express*, 2010, **18**, 16492–16498.
38 N. Papasimakis, Z. Luo, Z. X. Shen, F. De Angelis, E. Di Fabrizio, A. E. Nikolaenko and N. I. Zheludev, *Opt. Express*, 2010, **18**, 8353–8359.
39 T. Liu, H. Wang, Y. Liu, L. Xiao, C. Zhou, Y. Liu, C. Xu and S. Xiao, *J. Phys. D: Appl. Phys.*, 2018, **51**, 415105.
40 S. Xiao, T. Wang, X. Jiang, X. Yan, L. Cheng, B. Wang and C. Xu, *J. Phys. D: Appl. Phys.*, 2017, **50**, 195101.
41 S. Xiao, T. Liu, C. Zhou, X. Jiang, L. Cheng and C. Xu, *J. Opt. Soc. Am. B*, 2019, **36**, E48–E54.
42 S. Xiao, T. Wang, T. Liu, X. Yan, Z. Li and C. Xu, *Carbon*, 2018, **126**, 271–278.
43 Y. K. Srivastava, A. Chaturvedi, M. Manjappa, A. Kumar, G. Dayal, C. Kloc and R. Singh, *Adv. Opt. Mater.*, 2017, **5**, 1700762.
44 Y. Hu, T. Jiang, J. Zhou, H. Hao, H. Sun, H. Ouyang, M. Tong, Y. Tang, H. Li, J. You, X. Zheng, Z. Xu and X. Cheng, *Nano Energy*, 2020, **68**, 104280.
45 K. Shportko, S. Kremers, M. Woda, D. Lencer, J. Robertson and M. Wuttig, *Nat. Mater.*, 2008, **7**, 653.
46 P. Hosseini, C. D. Wright and H. Bhaskaran, *Nature*, 2014, **511**, 206.
47 S.-H. Lee, Y. Jung and R. Agarwal, *Nat. Nanotechnol.*, 2007, **2**, 626.
48 M. Wuttig and N. Yamada, *Nat. Mater.*, 2007, **6**, 824.
49 C. D. Wright, Y. Liu, K. I. Kohary, M. M. Aziz and R. J. Hicken, *Adv. Mater.*, 2011, **23**, 3408–3413.
50 H. F. Hamann, M. O'Boyle, Y. C. Martin, M. Rooks and H. K. Wickramasinghe, *Nat. Mater.*, 2006, **5**, 383.
51 N. Yamada, E. Ohno, K. Nishiuchi, N. Akahira and M. Takao, *J. Appl. Phys.*, 1991, **69**, 2849–2856.
52 C. M. Chang, C. H. Chu, M. L. Tseng, H.-P. Chiang, M. Mansuripur and D. P. Tsai, *Opt. Express*, 2011, **19**, 9492–9504.
53 R. Pandian, B. J. Kooi, G. Palasantzas, J. T. De Hosson and A. Pauza, *Adv. Mater.*, 2007, **19**, 4431–4437.
54 M. Terao, T. Morikawa and T. Ohta, *Jpn. J. Appl. Phys.*, 2009, **48**, 080001.
55 D. Loke, T. Lee, W. Wang, L. Shi, R. Zhao, Y. Yeo, T. Chong and S. Elliott, *Science*, 2012, **336**, 1566–1569.
56 B. Gholipour, J. Zhang, K. F. MacDonald, D. W. Hewak and N. I. Zheludev, *Adv. Mater.*, 2013, **25**, 3050–3054.
57 K. Du, L. Cai, H. Luo, Y. Lu, J. Tian, Y. Qu, P. Ghosh, Y. Lyu, Z. Cheng, M. Qiu and Q. Li, *Nanoscale*, 2018, **10**, 4415–4420.
58 Y. Qu, Q. Li, L. Cai, M. Pan, P. Ghosh, K. Du and M. Qiu, *Light: Sci. Appl.*, 2018, **7**, 26.
59 K. K. Du, Q. Li, Y. B. Lyu, J. C. Ding, Y. Lu, Z. Y. Cheng and M. Qiu, *Light: Sci. Appl.*, 2017, **6**, e16194.
60 Y. Qu, Q. Li, K. Du, L. Cai, J. Lu and M. Qiu, *Laser Photonics Rev.*, 2017, **11**, 1700091.
61 T. Cao, X. Zhang, W. Dong, L. Lu, X. Zhou, X. Zhuang, J. Deng, X. Cheng, G. Li and R. E. Simpson, *Adv. Opt. Mater.*, 2018, 1800169.
62 C. Choi, S. Y. Lee, S. E. Mun, G. Y. Lee, J. Sung, H. Yun, J. H. Yang, H. O. Kim, C. Y. Hwang and B. Lee, *Adv. Opt. Mater.*, 2019, 1900171.
63 C. Li, W. Zhu, Z. Liu, S. Yan, R. Pan, S. Du, J. Li and C. Gu, *Appl. Phys. Lett.*, 2018, **113**, 231103.
64 J. Tian, H. Luo, Y. Yang, F. Ding, Y. Qu, D. Zhao, M. Qiu and S. I. Bozhevolnyi, *Nat. Commun.*, 2019, **10**, 396.
65 E. Petronijevic and C. Sibilia, *Opt. Express*, 2016, **24**, 30411–30420.

66 W. Zhu, R. Yang, Y. Fan, Q. Fu, H. Wu, P. Zhang, N.-H. Shen and F. Zhang, *Nanoscale*, 2018, **10**, 12054–12061.
67 A. Ahmadivand, B. Gerislioglu and N. Pala, *J. Phys. Chem. C*, 2017, **121**, 19966–19974.
68 C. H. Chu, M. L. Tseng, J. Chen, P. C. Wu, Y. H. Chen, H. C. Wang, T. Y. Chen, W. T. Hsieh, H. J. Wu and G. Sun, *Laser Photonics Rev.*, 2016, **10**, 986–994.
69 D. Aspnes, *Am. J. Phys.*, 1982, **50**, 704–709.
70 V. A. Fedotov, M. Rose, S. L. Prosvirnin, N. Papasimakis and N. I. Zheludev, *Phys. Rev. Lett.*, 2007, **99**, 147401.
71 N. M. Sundaresan, Y. Liu, D. Sadri, L. J. Szöcs, D. L. Underwood, M. Malekakhlagh, H. E. Türeci and A. A. Houck, *Phys. Rev. X*, 2015, **5**, 021035.
72 K. Koshelev, S. Lepeshov, M. Liu, A. Bogdanov and Y. Kivshar, *Phys. Rev. Lett.*, 2018, **121**, 193903.
73 M. Liu, D. Powell, I. Shadrivov, M. Lapine and Y. S. Kivshar, *New J. Phys.*, 2013, **15**, 073036.
74 N. Papasimakis, V. A. Fedotov, N. Zheludev and S. Prosvirnin, *Phys. Rev. Lett.*, 2008, **101**, 253903.
75 M. Manjappa, S.-Y. Chiam, L. Cong, A. A. Bettiol, W. Zhang and R. Singh, *Appl. Phys. Lett.*, 2015, **106**, 181101.
76 Y. Fan, F. Zhang, N.-H. Shen, Q. Fu, Z. Wei, H. Li and C. M. Soukoulis, *Phys. Rev. A*, 2018, **97**, 033816.
77 B. Gallinet, T. Siegfried, H. Sigg, P. Nordlander and O. J. Martin, *Nano Lett.*, 2013, **13**, 497–503.
78 A.-K. U. Michel, P. Zalden, D. N. Chigrin, M. Wuttig, A. M. Lindenberg and T. Taubner, *ACS Photonics*, 2014, **1**, 833–839.